Permanent Electride Magnets Induced by Quasi-Atomic Non-Nucleus-Bound Electrons

Jeong Yun Hwang, Seung Yong Lee, Kimoon Lee, Binod Regmi, Nahyun Lee, Dong Cheol Lim, Heejeong Koo, Wooyoung Lee,* Seong-Gon Kim,* Sung Wng Kim,* and Kyu Hyoung Lee*

Interstitial quasi-atomic electrons (IQEs) in the quantized energy levels of positively charged cavities possess a substantial own magnetic moment and control the magnetism of crystalline electrides depending on the interaction with surrounding cations. However, weak spin-orbit coupling and gentle exchange interaction restricted by the IQEs preclude a large magnetic anisotropic, remaining a challenge for a hard magnetism. It is reported that 2D $[Re_2C]^{2+}\cdot2e^-$ electrides (Re = Er, Ho, Dy, and Tb) show the permanent magnetism in a ferrimagnetic ground state, mimicking the ferrites composed of magnetic sublattices with different spin polarizations. Magnetic interaction between Re-spin lattice and IQE-spin lattice in the $[Re_2C]^{2+}\cdot2e^-$ electrides results in a large magnetocrystalline anisotropy and high coercivity, giving a maximum energy product of 15 MGOe. It is demonstrated that the spontaneous breaking of magnetic IQE-sublattice through substitution with paramagnetic elements produces a crossover into an antiferromagnetic spin ordering of Re-sublattice, implying that the magnetic sublattice of IQEs drives the permanent magnetism.

1. Introduction

Electron has an intrinsic magnetic dipole aligned with internal angular momentum that is a spin. Because a single electron is an elementary particle with spin magnetic moment of 1/2 and thus regarded as a tiny magnet itself, its interaction with other electrons controls their magnetic dipole orientation, defining a magnetism.[1–3] This fundamental principle has been experimentally demonstrated by measuring the magnetic interactions of non-nucleus-bound electrons of separated ions,[4,5] which contributes the knowledge on the electron spin entanglement in quantum technology. Such non-nucleus-bound electrons are often found in the conventional ionic materials, where a crystallographic vacancy defect of an anion is occupied by one or more unpaired electrons (F-center),[6,7] but generally passive in imparting practical magnetic properties.[8–10] However, interstitial anionic electrons (IAEs) with the non-nucleus-bound nature, which construct ionic crystalline electrides as an essential ingredient together with positively charged lattice framework and clearly distinguishes from non-nucleus-bound electrons trapped in color center defects of ionic compounds,[11–16] have been identified as magnetic electrons with a substantial spin moment for dominating the magnetic properties of electrides.[13]

In 2D electrides, the IAEs are strongly localized between positively charged layers and occupy specific crystallographic Wyckoff positions, behaving as magnetic quasi-atoms.[17–30] These interstitial quasi-atomic electrons (I play as ferromagnetic elements in the $[Y_2C]^{2+}\cdot2e^-$ and $[Gd_2C]^{2+}\cdot2e^-$ electrides,[18,20] rendering the superparamagnetism in the paramagnetic $[Y_2C]^{2+}$ and the soft ferromagnetism in antiferromagnetic $[Gd_2C]^{2+}$ lattice framework, respectively. However, because the spin moments of the IQEs in magnetic electrides are small, their mutual exchange

J. Y. Hwang, S. Y. Lee, W. Lee, K. H. Lee
Department of Materials Science and Engineering
Yonsei University
Seoul 03722, Republic of Korea
E-mail: wooyoung@yonsei.ac.kr; khlee2018@yonsei.ac.kr
J. Y. Hwang, S. Y. Lee
KIURI Institute
Yonsei University
Seoul 03722, Republic of Korea
K. Lee
Department of Physics
Kunsan National University
Gunsan 54150, Republic of Korea

B. Regmi, S.-G. Kim
Department of Physics & Astronomy and Center for Computational Sciences
Mississippi State University
Mississippi States, Mississippi 39762, USA
E-mail: sk162@msstate.edu
N. Lee, D. C. Lim, H. Koo, S. W. Kim
Department of Energy Science
Sungkyunkwan University
Suwon 16419, Republic of Korea
E-mail: kimsungwng@skku.edu
S. W. Kim
Center for Innovative Electride Materials
Sungkyunkwan University
Suwon 16419, Republic of Korea

**ADVANCED
SCIENCE NEWS**

www.advancedsciencenews.com

**ADVANCED
MATERIALS**

www.advmat.de
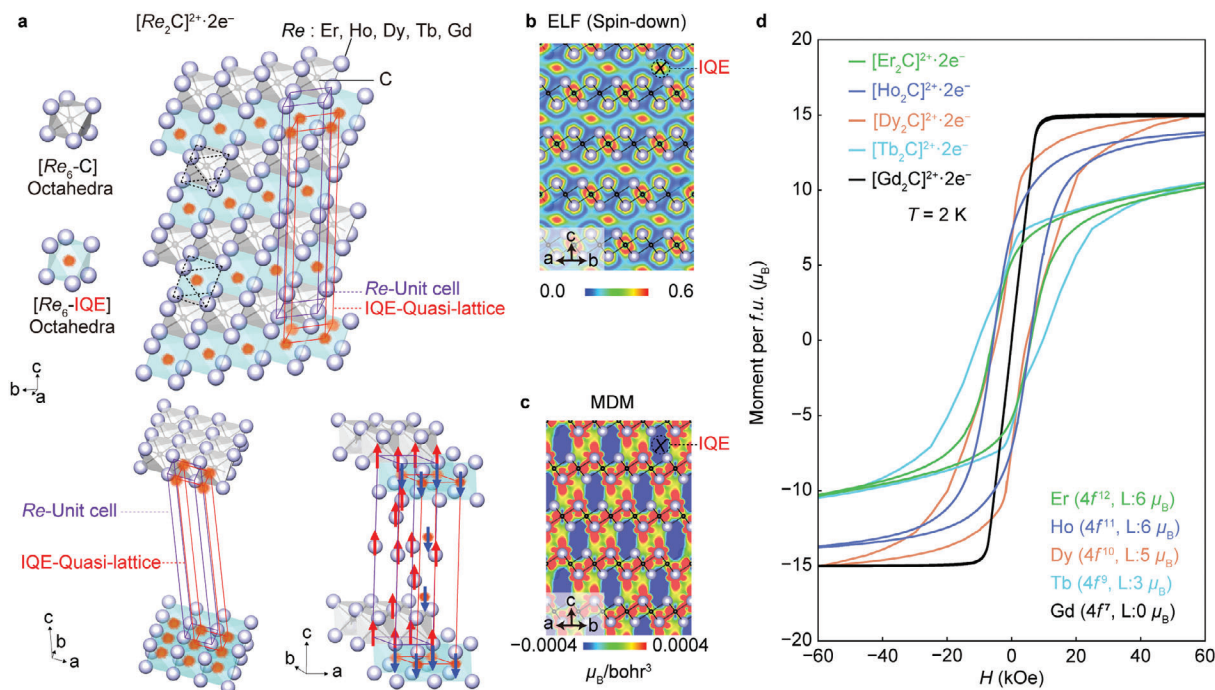
Figure 1. Magnetic ferrite of $[Re_2C]^{2+}\cdot 2e^-$ electride from $[Re_2C]^{2+}$ and IQE sublattice. a) Crystal structure of $[Re_2C]^{2+}\cdot 2e^-$ electride (Re: Er, Ho, Dy, Tb, and Gd) with unit cell IQE-Quasi-lattice (Red) and Re-Unit cell (Purple). (Derived by XRD results in Figure S1 and Table S1, Supporting Information). The left side of $[Re_2C]^{2+}\cdot 2e^-$ electride crystal structure displays the octahedral structure of $[Re_6C]$ and $[IQE-Re_6]$. The bottom left crystal structure schematically illustrates the overlapped sublattices and the bottom right structure represents the spin configuration of IQE-quasi lattice and Re-unit cell in $[Re_2C]^{2+}\cdot 2e^-$ electride crystal structure. b) 2D contour plot of ELF map for spin-down electron representing the localization (ELF) of IQEs along (110) direction of $[Er_2C]^{2+}\cdot 2e^-$ electride (Spin-up ELF in Figure S2, Supporting Information). c) MDM results (Red color is spin-up and blue is spin-down, $[Ho_2C]^{2+}\cdot 2e^-$ MDM result is in Figure S3, Supporting Information). The X in dot circles indicates the IQE position at the (110) plane. Schematic illustrated sliced plane in Figure S5 (Supporting Information). d) Field dependence magnetic moment curve of $[Re_2C]^{2+}\cdot 2e^-$ electride at 2K.

interactions are small enough so that the hybridization between IQEs and orbital electrons of neighboring cations with higher local moments is a key mechanism underlying the magnetism of electrides. This can be revisited by stimulating the spin-orbit interaction from the compositional design of electrides with an element having a high orbital angular momentum that enables a hard magnetism, although such magnetic electride has not been realized in any compounds, nor conceived by any theoretical suggestions. In this article, we prepared and examined a series of 2D rare earth carbide electrides, $[Re_2C]^{2+}\cdot 2e^-$ (Re = Er, Ho, Dy, and Tb), which are crystallized in anti-CdCl$_2$-type layered structure, bearing the IQEs in the interlayer space. Employing the heavy rare earth elements with substantial spin and orbital angular moments renders an exotic spin structure that is composed of two magnetic sublattices of cationic rare earth elements and quasi-atomic IQEs. This unprecedented spin structure results in a large magnetic hysteresis and a high coercive field as characteristic features of permanent magnets, which have never been observed in magnetic electrides, to the best of our knowledge.

2. Results

2.1. Permanent Magnetic $[Re_2C]^{2+}\cdot 2e^-$ Electrides

The rhombohedral $[Re_2C]^{2+}\cdot 2e^-$ electrides consist of alternating cationic $[Re_2C]^{2+}$ layers and anionic IQEs layers, where the oc-

tahedral Re_6C units construct the cationic layer from the mixed ionic and covalent bonds between Re^{3+} and C^{4-} ions (**Figure 1a**). Two excess IQEs ($2e^-$) occupy the interlayer 2D space to maintain a charge neutrality and stabilize the rhombohedral structure. It can be postulated that the IQEs form another octahedral Re_6IQE polyhedron with six nearest neighbor Re^{3+} cations in the $[Re_2C]^{2+}$ layers, satisfying the nature of electrides. From the theoretical calculations for the (110) plane of $[Er_2C]^{2+}\cdot 2e^-$ electride as a representative system (Figure 1b and Figure S2, Supporting Information), the difference of electron localization function (ELF) for spin-up and -down clearly shows that the IQEs are strongly localized at the centre positions of the octahedra between the cationic layers, occupying the Wyckoff positions of (0 0 1/2) that is displaced by (0 0 1/2) from the positions of the Re cations. This result is exactly identical to every ELFs of the reported 2D electrides.[18,20] However, the magnetic spin configuration is apparently different from the ever-reported magnetic electrides. It should be noted from the calculated magnetic density map (MDM) (Figure 1c and Figures S3,S4, Supporting Information) that the spin states of the Re cations in the $[Re_2C]^{2+}$ cationic layers and IQEs in the interlayer are distinguishable, exhibiting spin-up (red) and spin-down (blue) states, respectively. Given the fact that the strongly localized IQEs in the octahedral Re_6IQE units possess their own magnetic moments, the IQEs can be also considered as magnetic quasi-atoms. Most of all, the intriguing spin structure is reminiscent of ferrite permanent

**ADVANCED
SCIENCE NEWS**

www.advancedsciencenews.com

**ADVANCED
MATERIALS**

www.advmat.de

magnets, which are disassembled into individual magnetic sublattices of constituent cations (Fe^{3+} and Fe^{4+}) with inequivalent spin states.[1,2,31] Such scheme of magnetic sublattices is also applicable to the rhombohedral $[Re_2C]^{2+}\cdot 2e^-$ electrides with cationic Re- and anionic IQE-sublattices with antiparallel alignment of magnetic moments (Figure 1c and Figure S6, Supporting Information).

Antiparallel-aligned magnetic sublattices of cationic Re and anionic IQE are responsible for the first observed hysteresis in magnetization curves of the $[Re_2C]^{2+}\cdot 2e^-$ electrides (Figure 1d). Unlike the weak ferromagnetic $[Gd_2C]^{2+}\cdot 2e^-$ electride,[20] where the magnetic IQEs are aligned in the same direction with the spins of Gd cations, all the present $[Re_2C]^{2+}\cdot 2e^-$ electrides obviously exhibit a substantial coercive force, indicating the unprecedented permanent magnetism in the electride research. The magnetization curves of all the $[Re_2C]^{2+}\cdot 2e^-$ electrides show the saturation magnetization in common, but different H_c values depending on the Re elements. Considering the distinct difference between $[Re_2C]^{2+}\cdot 2e^-$ and $[Gd_2C]^{2+}\cdot 2e^-$ electrides, the exchange interaction processes between magnetic IQEs and nearby magnetic cations are largely dominated by the degree of spin-orbit coupling, which can be modulated according to the magnetic cations with spin and orbital angular moments. More strictly, such difference can be attributed to the non-zero orbital angular moments of Re elements in contrary to zero orbital angular moment of gadolinium, which originates from the half-filled $4f^7$ shell with spherically symmetric charge distribution for minimizing the orbital contribution to the magnetic moment and consequently resulting in a lower magnetic anisotropy than the other $[Re_2C]^{2+}\cdot 2e^-$ electride.

2.2. Ferrimagnetism of the $[Re_2C]^{2+}\cdot 2e^-$ Electrides

Temperature dependent magnetization curves of the 2D electrides show that a magnetic phase transition occurs at different temperatures according to the rare earth elements and a divergence between zero-field-cooling (ZFC) and field-cooling (FC) magnetization curves appears in all the $[Re_2C]^{2+}\cdot 2e^-$ electrides except the ferromagnetic $[Gd_2C]^{2+}\cdot 2e^-$ electride (**Figure 2a**). The Curie–Weiss fittings of the FC magnetizations for the 2D electrides gives the Curie temperature (T_C) (Figure 2b and Figure S7a, Supporting Information (dM/dT)). It is obvious that the variation of the T_C strongly depends on the species of Re cations in the 2D electrides, where a higher T_C emerges in an electride composed of a Re element with larger spin moment (Figure S7b, Supporting Information). The divergence between ZFC and FC magnetizations can be originated from the antiparallel spin ordering, which is proved by the decrease of magnetic transition temperature (T^*) in ZFC magnetization with the increase in the magnetic field (H), as observed in $[Er_2C]^{2+}\cdot 2e^-$ and $[Ho_2C]^{2+}\cdot 2e^-$ (Figure S8, Supporting Information). The deviations from Curie–Weiss fittings (depicted with gray color) also supports the antiparallel spin ordering of the all permanent $[Re_2C]^{2+}\cdot 2e^-$ electrides (Figure 2b). Furthermore, the constant phase transition temperature (noted as T^* and T_C) under different frequencies on the imaginary part of AC susceptibility confirms the intrinsic nature of long-range magnetic ordering, excluding a possibility of short-range orderings such as spin-glass and impurities ef-

fect (Figure 2c,d). Thus, considering together both the theoretical MDM plot (Figure 1c) and the measured magnetic properties, we conclude that the present permanent magnetic $[Re_2C]^{2+}\cdot 2e^-$ electrides is ferrimagnetic. Additionally, we verify the ground state of the $[Re_2C]^{2+}\cdot 2e^-$ electrides, which is also revealed to be ferrimagnetic, showing a significantly lower total energy than that of antiferromagnetic ordering by ≈6 eV per f.u., as shown in Figure S9 (Supporting Information).

2.3. Large Magnetocrystalline Anisotropy and Coercivity Beyond Hard Ferrite Magnets

The exceptionally high intrinsic coercive force (H_{ci}) of the permanent magnetic $[Re_2C]^{2+}\cdot 2e^-$ electrides is the most intriguing feature originated from the antiparallel-aligned magnetic Re- and IQE-sublattices. In order to elucidate the origin for the presence of H_{ci} in 2D electrides, we estimate a magnetic anisotropy constant (K_1) by the approach to saturation fitting (red dotted lines) as shown in **Figure 3a**. While the weak ferromagnetic $[Gd_2C]^{2+}\cdot 2e^-$ electride show the K_1 value of ≈1 MJ m^{-3}, all the permanent magnetic $[Re_2C]^{2+}\cdot 2e^-$ electrides show the K_1 value exceeding 2 MJ m^{-3}, reaching to the 6 MJ m^{-3} for the $[Dy_2C]^{2+}\cdot 2e^-$ electride, which is much higher value than those of ever-reported ferrite magnets.[31–34] These extraordinary K_1 values can be ascribed to strong spin-orbit coupling (SOC) of magnetic Re cations and IQEs. Although the accurate relationship between K_1 and SOC is still being proven depending on models, many theoretical and experimental results have demonstrated that the SOC is proportional to K_1.[35–41] The SOC Hamiltonian is

$$H_{SOC} = \xi L \cdot S \tag{1}$$

where L and S are the orbital angular momentum and spin angular momentum, and ξ is the spin-orbit coupling constant. The magnetocrystalline anisotropy energy (E_{MAE}) is defined by difference between the two total energies where the spin quantization axes are aligned toward two different directions as

$$E_{MAE} = E_{(100)} - E_{(001)} \tag{2}$$

$E_{(100)}$ and $E_{(001)}$ are the total energy with spin quantization axis in the magnetically hard plane and easy axis, respectively. The relationship between anisotropy constant (K_1 and K_2) and E_{MAE} is described as
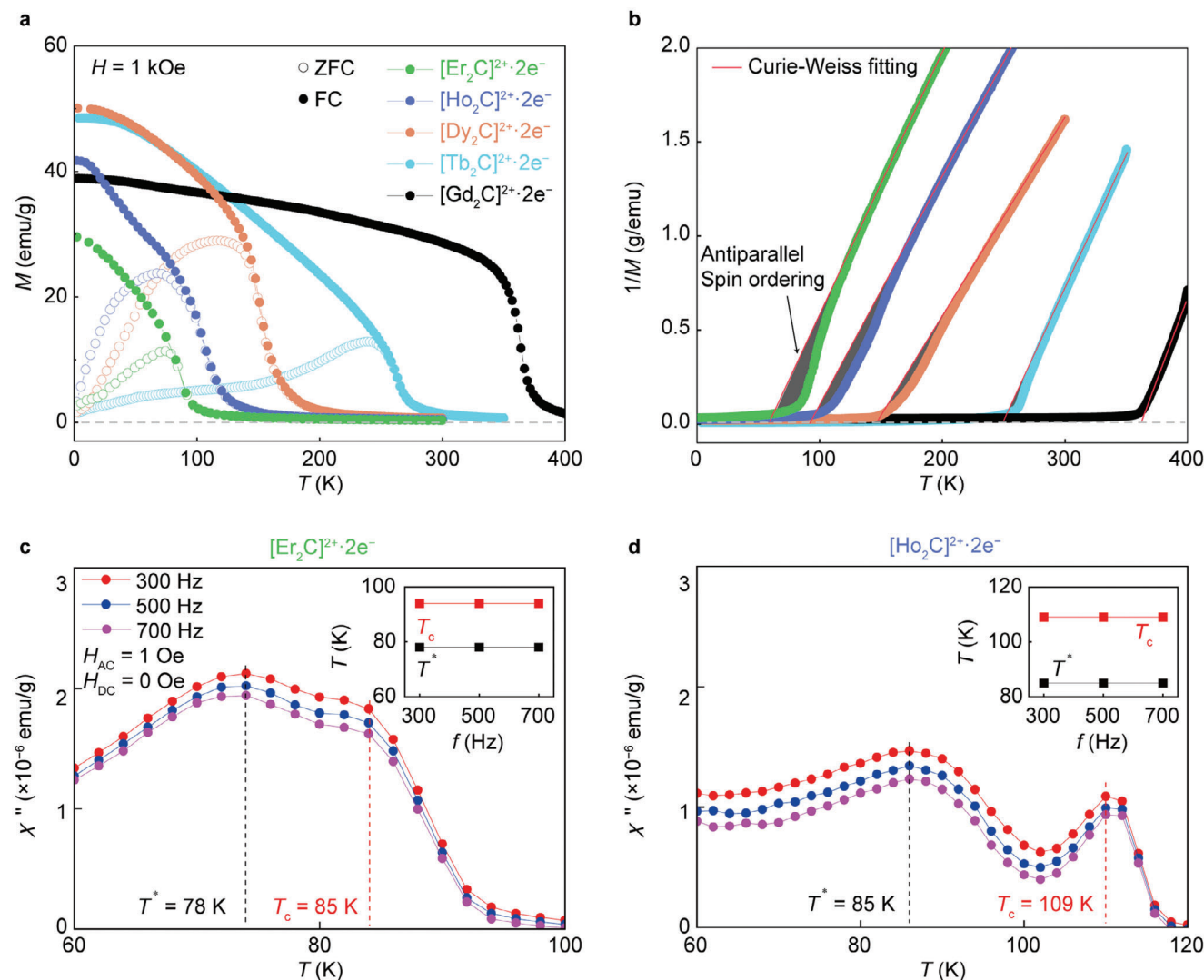
$$E_{MAE} = K_1 \sin^2\theta + K_2 \sin^4\theta \tag{3}$$

$$K_1 = \frac{E_{MAE}}{V Sin^2\theta} \approx E_{MAE}/V \tag{4}$$

The V is the equilibrium volume of the unit cell, and θ is the angle between the two spin quantization axis orientations. The K_1 also can be expressed with anisotropy field (H_a) and saturation magnetization (M_s) as

$$H_a = \frac{2K_1}{M_s} \tag{5}$$

The relation of E_{MAE} and K_1 value is established by Equations (3) and (4), where K_1 and K_2 are the uniaxial anisotropy

**ADVANCED
SCIENCE NEWS**

www.advancedsciencenews.com

**ADVANCED
MATERIALS**

www.advmat.de

Figure 2. Temperature-dependent magnetization curve. a) Temperature dependence magnetization curve of $[Re_2C]^{2+}\cdot 2e^-$ electride (Re: Er, Ho, Dy, Tb, and Gd) under 1 kOe. The open circle is ZFC and the closed circle is FC. b) Results of Curie–Weiss law fitting (Red curve). The black plane indicates the antiparallel spin ordering signal. The imaginary AC susceptibility results under different frequencies. c) $[Er_2C]^{2+}\cdot 2e^-$. d) $[Ho_2C]^{2+}\cdot 2e^-$ electride. The inset displays the constant phase transition temperature under different AC frequencies. The T^* is phase transition of antiparallel spin ordering and T_C.

constants. Thus, the K_1 is proportional to the multiplication of spin and orbital angular moments of each magnetic element, in which the gadolinium is the only element with zero orbital angular moment among rare earth elements, it is evident that the Re cations with non-zero orbital angular moments are highly responsible to induce the magnetocrystalline anisotropy for the high H_{ci} of the permanent magnetic $[Re_2C]^{2+}\cdot 2e^-$ electrides. However, it is elusive on the contribution of the IQEs to the SOC for the large magnetocrystalline anisotropy. Nevertheless, the MAE values of $[Er_2C]^{2+}\cdot 2e^-$, $[Ho_2C]^{2+}\cdot 2e^-$, and $[Gd_2C]^{2+}\cdot 2e^-$ electrides have been calculated to compare the difference between permanent magnetic and soft-ferromagnetic electrides (Table S2, Supporting Information). It is clearly demonstrated that the both permanent magnetic $[Er_2C]^{2+}\cdot 2e^-$ and $[Ho_2C]^{2+}\cdot 2e^-$ represent more than 2-3 orders higher of MAE values than soft-

ferromagnetic $[Gd_2C]^{2+}\cdot 2e^-$ electride. In order to characterize the permanent magnetic $[Re_2C]^{2+}\cdot 2e^-$ electrides, we plot the magnetic field dependences of magnetic flux density (B) and maximum energy product (($BH)_{max}$) as shown in Figure 3b,c, respectively. Surprisingly, the ($BH)_{max}$ values are ranged from 8 MGOe of $[Dy_2C]^{2+}\cdot 2e^-$–15 MGOe of $[Ho_2C]^{2+}\cdot 2e^-$ and these values are much higher than those of conventional ferrite magnets (Figures S10,S11, Supporting Information).[31–34] Note that the remarkable magnetic performance is achieved in the polycrystalline ingots of the $[Re_2C]^{2+}\cdot 2e^-$ electrides synthesized by a simple melt-solidification process (Methods). This gives a huge opportunity for maximizing the magnet performance of the permanent $[Re_2C]^{2+}\cdot 2e^-$ magnets following the established strategies for enhancing the ($BH)_{max}$ value of permanent magnets such as boundary engineering and nanostructuring.[1,2,42]
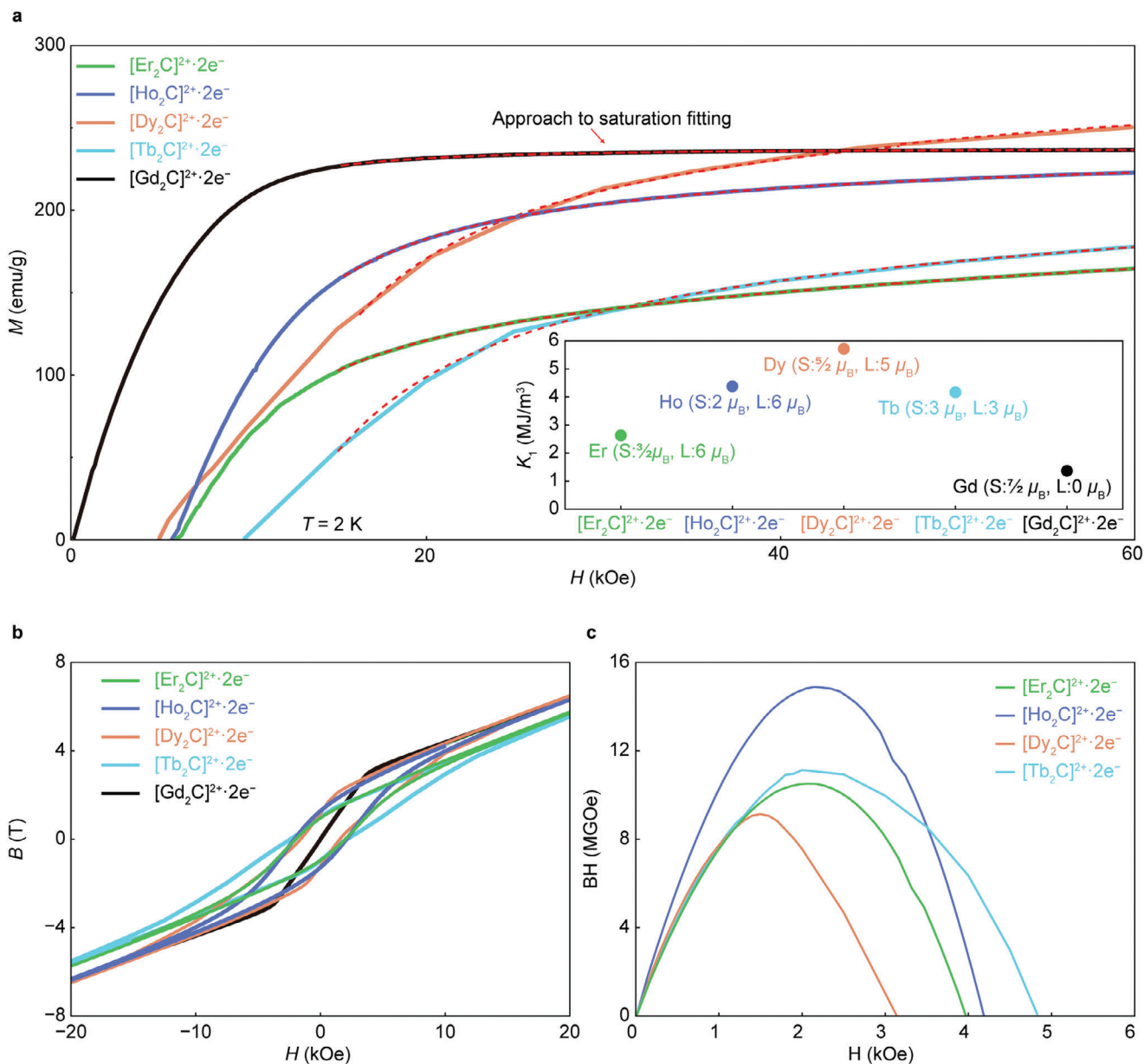
Figure 3. Permanent magnet $[Re_2C]^{2+} \cdot 2e^-$ electride. a) Results of the approach to saturation fitting. The derived K_1 values are noted in the inset plot. b) B-H curve of $[Re_2C]^{2+} \cdot 2e^-$ electride. c) Maximum energy product depending on magnetic field curve (BH-H curve) of hard ferrite $[Re_2C]^{2+} \cdot 2e^-$ electride.

2.4. Spin-Orbit Coupling of Magnetic Re and IQEs

In all magnetic electrides, the IQEs have played a dominant role in imparting the magnetism of electrides as ferromagnetic elements interacting with neighboring cations. Though the exchange interactions between Re cations and IQE anions determine their spin arrangements for the ferrimagnetism, it is important to answer which magnetic ions are a key ingredient for the permanent magnetism and how they induce the exceptionally high H_{ci}. Apart from the theoretical expectation that may remain the uncertainty on physical parameters of non-nucleus-bound electrons, that is the IQEs, we have experimentally proved that the presence of the IQEs trigger the magnetocrystalline anisotropy,

forming the magnetic quasi-lattice. **Figure 4** shows that the spontaneous breakdown of the IQE-sublattice accompanying the decrease in electron density leads to the loss of the intrinsic coercive force. Substituting the magnetic IQEs with the paramagnetic chlorine and hydrogen atoms reduces the T_C and the magnitude of the divergence between ZFC and FC magnetizations in permanent magnetic $[Er_2C]^{2+} \cdot 2e^-$ electride (Figure 4a). From the structural analyses on the Cl- and H-substituted Er$_2$C compounds (Figures S12,S13, Supporting Information) and the references of the previously reported Cl- and H-substituted Gd$_2$C compounds,[20,22] it is obvious that the density of the IQEs can be decreased by the occupation of Cl and H ions at the original Wyckoff positions of the IQEs. We examined the chlorinated

**ADVANCED
SCIENCE NEWS**

www.advancedsciencenews.com

**ADVANCED
MATERIALS**

www.advmat.de
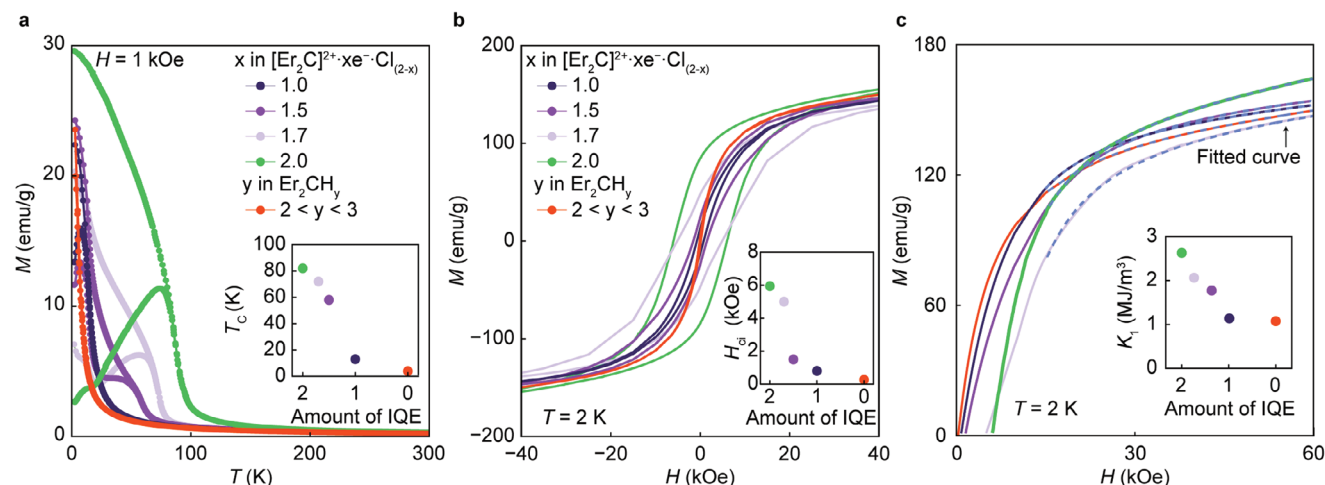
Figure 4. Permanent magnetic properties depending on the density (x) of the IQEs. a) M-T curves depending on the IQE amount in $[Er_2C]^{2+} \cdot 2e^-$, $[Er_2C]^{2+} \cdot xe^- \cdot Cl_{(2-x)}$ ($1 \leqq x \leqq 2$) and Er_2CH_y ($2 < y < 3$). Inset is the plot of T_C versus the amount of IQE. b) M-H curves. The decreased H_{Ci} depending on the IQE amount is plotted in inset. c) Fitting for K_1 value from M-H curves. Inset demonstrates the decreased K_1 according to the amount of IQE.

$[Er_2C]^{2+} \cdot xe^- \cdot Cl_{2-x}$ ($1 \leqq x \leqq 2$) and hydrogenated Er_2CH_y ($2 < y < 3$) compounds, where the density of the IQEs can be decreased to one mole and zero, respectively. Depending on the amounts of Cl and H, a systematic change of T_C is clearly shown in the dM/dT (Figure S14b, Supporting Information) and the contribution of the IQEs for the ferrimagnetism is largely depressed as shown in the Curie–Weiss fitting (Figure S14, Supporting Information).

Figures 4B,C explicitly verify that the presence of the IQEs triggers the permanent magnetism in the $[Re_2C]^{2+} \cdot 2e^-$ electrides. The H_{ci} value decreases with the increase of the Cl amount and completely disappears in the hydrogenated Er_2CH_y ($2 < y < 3$) compound, which indicates the absence of the IQE-sublattice. While the ferromagnetic $[Gd_2C]^{2+} \cdot 2e^-$ electride shows the canted-antiferromagnetic ordering with the replacement of the IQEs by Cl and H (Figure S15, Supporting Information), the hydrogenated Er_2CH_y ($2 < y < 3$) compound shows a weak ferromagnetic feature. The estimation of K_1 values by the approach to saturation fitting (blue dotted lines in Figure 4c) also indicates that the Er_2CCl_x ($x = 1.0$) and Er_2CH_y compounds are far from the permanent magnets, showing a similar value to that of the weak ferromagnetic $[Gd_2C]^{2+} \cdot 2e^-$ electride. Importantly, from the experimental evidence that the saturation magnetizations of $[Er_2C]^{2+} \cdot 2e^-$ electride and Cl- and H-substituted Er_2C compounds are almost unchanged (measured magnetic moment is depicted in Figures S16,S17, Supporting Information) in spite of the dramatic change in the H_{ci} and K_1 values (Figure 4b,c), it is indisputable that the higher magnetocrystalline anisotropy in the permanent $[Er_2C]^{2+} \cdot 2e^-$ electride emerges from the presence of the IQEs and SOC with Er. According to the dependence of magnetic properties on magnetization direction, magnetization density of the IQEs can be pronounced in the (001) magnetic field direction compared to the (100) direction, implying the hybridization between Re and IQE in the (001) direction is critical (Figure S18 and Table S3, Supporting Information). Thus, because the IQEs are hybridized with atomic orbitals of neighbour Re cations (Figure S19, Supporting Information), the SOC of the magnetic Re cations can be expected to be correlatively pronounced with the magnetic IQEs. Furthermore, the magnetic IQEs bridging the Re

cations with non-zero orbital angular moment are the key ingredient to induce the magnetocrystalline anisotropy for realizing the permanent magnetic electrides.

3. Conclusion

Herein, we experimentally demonstrated that permanent magnetism can be induced by IQEs between cations in the simultaneous presence of inherent spin moment and orbital coupling, originating from the structural stabilization due to charge neutrality in rare earth carbide electride. The ferrite-like spin structure results from the antiparallel spin alignments of each magnetic sublattice composed of rare earth cations and IQEs, which generates a ferrimagnetic phase and enhances the magnetic anisotropy. The clear identification of the role and nature of the IQEs in magnetic electrides raises an intriguing question that non-nucleus-bound electrons can exhibit a substantial orbital angular moment in a quasi-lattice. Further studies on the single crystal and magnetic anisotropy of permanent magnet electrides will be an important step toward identifying the intrinsic orbital angular moment of the IQEs. Finally, this work initiates a further development of room-temperature permanent magnetic electrides by engineering the composition and domain structure to allow the manipulation of magnetic anisotropy.

4. Experimental Section

Synthesis of $[Re_2C]^{2+} \cdot 2e^-$ Electride (Re = Er, Ho, Dy, Tb, and Gd): All samples were handled in glove boxes filled with high-purity argon gas (Ar 99.999%) to prevent the oxidation of lanthanide raw materials (Er, Ho, Dy, Tb, and Gd) and synthesized samples. The synthesis method of a polycrystalline ingot of $[Re_2C]^{2+} \cdot 2e^-$ electrides was performed by the arc-melting process with mixed Er, Ho, Dy, Tb, or Gd metal pieces and graphite pieces in a 2:1 molar ratio under high-purity Ar atmosphere. The synthesized electrides are unstable in air, changing their color from black to white (Figure S21, Supporting Information).

The Er_2CCl_x samples were synthesized by the solid-state reaction method by using pulverized $[Er_2C]^{2+} \cdot 2e^-$ powder, $ErCl_3$ (99.99%), and

**ADVANCED
SCIENCE NEWS**

www.advancedsciencenews.com

**ADVANCED
MATERIALS**

www.advmat.de

graphite. Pelletized mixed powders were wrapped with molybdenum foil and sealed in a quartz tube under 10^{-3} Pa. The vacuum-sealed quartz tube containing the pellet was annealed at 1000 °C for 72 h. in a box furnace. To synthesize the $Er_2CH_{2.y}$ composition, pelletized $[Er_2C]^{2+}\cdot2e^-$ electrides powder was placed in a quartz tube furnace under a 1 atm environment by 4% H_2/Ar mixed gas and heat treatment performed at 600 K for 72 h.

Structural Characterization by XRD Measurement: The crystal structure of the synthesized $[Re_2C]^{2+}\cdot2e^-$ electride samples were investigated by XRD using a Rigaku SmartLab diffractometer with monochromatic Cu Kα radiation (8.04 keV) at room temperature. The well-ground powder samples were prepared in glove boxes and measured in a plastic dome-type stage filled with Ar gas to avoid oxidation during measurements. The crystal lattice parameters from obtained XRD patterns were analyzed by the General Structure Analysis System (GSAS) software package was applied to perform Rietveld refinement.

Magnetic and Electrical Properties Characterization: The sampling for resistivity and magnetic properties measurements were performed in the high-purity Ar-filled glove boxes. The temperature-dependent resistivity measurements were performed by the physical property measurement system (PPMS DynaCool, Quantum Design). The four-electrode was made using silver epoxy on the pelletized samples. After that, samples were covered with Apiezon *N* grease to block the oxidation during the sample loading to PPMS and measurements. The measurement of magnetic properties used a vibrating sample magnetometer (VSM, Quantum Design) and Squid magnetometer (MPMS3, Quantum Design) for AC magnetic susceptibility. A plastic capsule copula containing a weighted sample was coated with N grease to prevent the oxidation of samples.

The K_1 was derived by Law of approach to saturation, which was represented by following equations.

$$M = M_s \left[1 - \frac{a}{H} - \frac{b}{H^2} \right] + kH \tag{6}$$

The terms of *a* was magnetic hardness, which was attributed by defects and dislocations in magnetic materials. The *b* was closely related to K_1 as following equation.

$$b = \frac{8}{105} \frac{K_1^2}{M_s^2} \tag{7}$$

To derive the K_1 value of $[Re_2C]^{2+}\cdot2e^-$ electrides, Er_2CCl_x and $Er_2CH_{2.y}$, we perform the fitting from 1.5 to 6.0 T of range in M–H curve of each sample by using Law of approach to saturation equations.

Computational Method: All total energy calculations and geometry optimizations were performed based on first-principles spin-polarized density functional theory[43] as implemented by Kresse and Joubert[44] using the projector augmented-wave method.[45] The exchange-correlation functional was modeled using a generalized gradient approximation in the Perdew–Burke–Ernzerhof form.[46] All calculations were spin-polarized, and the positions of atoms and the size and shape of the unit cell were fully relaxed to obtain the optimized lattice structure. Additionally, we have taken into consideration the widely utilized van der Waals (vdW) correction (DFT-D3),[47] with the inclusion of SOC effect in all computations. Also, we have used DFT+U method for the $[Re_2C]^{2+}\cdot2e^-$ electrides. However, non-zero values for U in the DFT+U calculations did not reproduce the experimentally observed ferrimagnetic ordering of the present permanent magnetic electrides, showing a strong ferromagnetic feature, which was inconsistent with the experimental observations (Figure S3 and Table S4, Supporting Information). Calculation results of magnetization density map and moment were described in Figures S3, S4, S9, S16–S18, S22 and Table S5 (Supporting Information). Consequently, we set U to be zero and reported our calculation as DFT calculations. During the geometry relaxation of trigonal crystal structure of Er_2C bulk, all atoms were fully relaxed until the force on the atom was less than 0.001 eV/Å and the change in total energy was less than 10^{-5} eV. The electron wavefunctions were expanded in a plane-wave basis set with a cutoff energy of 520 eV, and bulk calculation was carried out by employing the reciprocal k-point mesh with

a density of $39/Å^{-3}$. The computed equilibrium lattice parameters for this setup were $a = b = 3.545Å$, and $c = 18.106Å$. For the ELF and magnetization density map calculations, the Brillouin zone was sampled using a denser k-point mesh with a density of $2492/Å^{-3}$. To obtain the projected density of states (PDOS) and band structure on the interstitial position ("X" site), an empty sphere having a Wigner–Seitz radius of $1.7Å$ was employed. The computation of the local magnetic moment for each ion, including the IQE, we used an extension of Bader's volume partitioning method[48] to accommodate magnetization densities that contain negative values.

Supporting Information

Supporting Information is available from the Wiley Online Library or from the author.

Conflict of Interest

The authors declare no conflict of interest.

Data Availability Statement

The data that support the findings of this study are available from the corresponding author upon reasonable request.

[1] R. C. O'handley, *Modern Magnetic Materials: Principles and Applications*, 1st ed., Wiley, New York, USA **1999**.

[2] B. D. Cullity, C. D. Graham, *Introduction to Magnetic Materials*, 2nd ed., Wiley, Hoboken, USA **2008**.

[3] G. Breit, *Nature* **1928**, *122*, 649.

[4] S. Kotler, N. Akerman, N. Navon, Y. Glickman, R. Ozeri, *Nature* **2014**, *510*, 376.

[5] D. Hanneke, S. Fogwell, G. Gabrielse, *Phys. Rev. Lett.* **2008**, *100*, 120801.

[6] J. J. Markham, *F-Centers in Alkali Halides*, Vol. 8, Academic Press, New York, USA **1966**.

[7] A. M. Portis, *Phys. Rev.* **1953**, *91*, 1071.

[8] R. Pentcheva, W. E. Pickett, *J. Phys.: Condens. Matter* **2010**, *22*, 043001.

[9] S. Banerjee, M. Mandal, N. Gayathri, M. Sardar, *Appl. Phys. Lett.* **2007**, *91*, 182501.

[10] V. I. Srdanov, G. D. Stucky, E. Lippmaa, G. Engelhardt, *Phys. Rev. Lett.* **1998**, *80*, 2449.

[11] J. L. Dye, *Science* **2003**, *301*, 607.

[12] J. L. Dye, *Science* **1990**, *247*, 663.

[13] J. L. Dye, *Acc. Chem. Res.* **2009**, *42*, 1564.

[14] M. Miyakawa, S. W. Kim, M. Hirano, Y. Kohama, H. Kawaji, T. Atake, H. Ikegami, K. Kono, H. Hosono, *J. Am. Chem. Soc.* **2007**, *129*, 7270.

[15] S. W. Kim, H. Hosono, *Philos. Mag.* **2012**, *92*, 2596.

[16] S. Matsuishi, Y. Toda, M. Miyakawa, K. Hayashi, T. Kamiya, M. Hirano, I. Tanaka, H. Hosono, *Science* **2003**, *301*, 626.

[17] K. Lee, S. W. Kim, Y. Toda, S. Matsuishi, H. Hosono, *Nature* **2013**, *494*, 336.

[18] J. Park, K. Lee, S. Y. Lee, C. N. Nandadasa, S. Kim, K. H. Lee, Y. H. Le, H. Hosono, S.-G. Kim, S. W. Kim, *J. Am. Chem. Soc.* **2017**, *139*, 615.

[19] J. Park, J.-Y. Hwang, K. H. Lee, S.-G. Kim, K. Lee, S. W. Kim, *J. Am. Chem. Soc.* **2019**, *139*, 17277.

[20] S. Y. Lee, J.-Y. Hwang, J. Park, C. N. Nandadasa, Y. Kim, J. Bang, K. Lee, K. H. Lee, Y. Zhang, Y. Ma, H. Hosono, Y. H. Lee, S.-G. Kim, S. W. Kim, *Nat. Commun.* **2020**, *11*, 1526.

[21] S. Liu, C. Wang, L. Liu, J.-H. Choi, H.-J. Kim, Y. Jia, C. H. Park, J.-H. Cho, *Phys. Rev. Lett.* **2020**, *125*, 187203.

[22] S. Y. Lee, D. C. Lim, M. S. Khan, J. Y. Hwang, H. S. Kim, K. H. Lee, S. W. Kim, *Nat. Commun.* **2023**, *14*, 5469.

[23] J. Zhou, J.-Y. You, Y.-M. Zhao, Y. P. Feng, L. Shen, *Acc. Chem. Res.* **2024**, *57*, 2572.

[24] J. Bu, H. Wu, J. Xu, S. Zhang, *J. Phys. Chem. C* **2023**, *127*, 14962.

[25] X. Zhang, W. Meng, Y. Liu, X. Dai, G. Liu, L. Kou, *J. Am. Chem. Soc.* **2023**, *145*, 5523.

[26] J. F. Zhang, D. Xu, X. L. Qiu, N. N. Zhao, Z. Y. Lu, K. Liu, *J. Phys. Chem. C* **2022**, *127*, 696.

[27] D. Xu, J. F. Zhang, Z. Y. Lu, K. Liu, *Phys. Rev. B* **2022**, *106*, 045138.

[28] X. Sui, J. Wang, C. Yam, B. Huang, *Nano Lett.* **2021**, *21*, 3813.

[29] H. Y. Song, B. I. Yoo, J.-H. Choi, S.-H. Kang, J. Bang, W. Li, C. N. Nandadasa, D. Thapa, D. Yoon, M. J. Han, K. H. Lee, S. G. Kim, K. Lee, S. W. Kim, *Mater. Today Phys.* **2021**, *20*, 100473.

[30] T. Inoshita, S. Jeong, N. Hamada, H. Hosono, *Phys. Rev. X* **2014**, *4*, 031023.

[31] A. Goldman, *Modern ferrite technology*, 2nd ed., Springer, Boston, USA **2006**.

[32] R. W. McCallum, L. H. Lewis, R. Skomski, M. J. Kramer, I. E. Anderson, *Annu. Rev. Mater. Res.* **2014**, *44*, 451.

[33] J. M. D. Coey, *IEEE Trans. Magn.* **2011**, *47*, 4671.

[34] D. Goll, H. Kronmüller, *Naturwissenschaften* **2000**, *87*, 423.

[35] A. Galler, S. Ener, F. Maccari, I. Dirba, K. P. Skokov, O. Gutfleisch, S. Biermann, L. V. Pourovskii, Q. Mater, **2021**, *6*, 2.

[36] R. Skomski, A. Kashyap, A. Enders, *J. Appl. Phys.* **2011**, *109*, 07E143.

[37] J. M. D. Coey, S. S. P. Parkin, *Handbook of Magnetism and Magnetic Materials*, 1st ed., Springer, Cham, Germany **2021**.

[38] L. Ke, *Phys. Rev. B* **2019**, *99*, 054418.

[39] X. Liang, X. Wu, J. Hu, J. Zhao, X. C. Zeng, *Commun. Phys.* **2018**, *1*, 74.

[40] P. Nieves, S. Arapan, J. Maudes-Raedo, R. Marticorena-Sánchez, N. L. Del Brío, A. Kovacs, C. Echevarria-Bonet, D. Salazar, J. Weischenberg, H. Zhang, O. Yu. Vekilova, R. Serrano-López, J. M. Barandiaran, K. Skokov, O. Gutfleisch, O. Eriksson, H. C. Herper, T. Schrefl, S. Cuesta-López, *Comput. Mater. Sci.* **2019**, *168*, 188.

[41] T. Liao, W. Xia, M. Sakurai, R. Wang, C. Zhang, H. Sun, K.-M. Ho, C.-Z. Wang, J. R. Chelikowsky, *Phys. Rev. Mater.* **2022**, *6*, 024402.

[42] J. Xu, K. Zhu, S. Gao, *Inorg. Chem. Front.* **2021**, *8*, 383.

[43] W. Kohn, L. J. Sham, *Phys. Rev.* **1965**, *140*, A1133.

[44] G. Kresse, D. Joubert, *Phys. Rev. B* **1999**, *59*, 1758.

[45] P. E. Blochl, *Phys. Rev. B* **1994**, *50*, 17953.

[46] J. P. Perdew, K. Burke, M. Ernzerhof, *Phys. Rev. Lett.* **1996**, *77*, 3865.

[47] S. Grimme, J. Antony, S. Ehrlich, H. Krieg, *J. Chem. Phys.* **2010**, *132*, 154104.

[48] R. F. W. Bader, *Acc. Chem. Res.* **1985**, *18*, 9.